



# Simulations of Water Vapor and Clouds on Rapidly Rotating and Tidally Locked Planets: A 3D Model Intercomparison

Jun Yang<sup>1,2</sup> , Jérémy Leconte<sup>3</sup> , Eric T. Wolf<sup>4</sup> , Timothy Merlis<sup>5</sup> , Daniel D. B. Koll<sup>6</sup> , François Forget<sup>7</sup>, and Dorian S. Abbot<sup>8</sup>

<sup>1</sup> Dept. of Atmospheric and Oceanic Sciences, School of Physics, Peking University, Beijing, 100871, People's Republic of China; [junyang@pku.edu.cn](mailto:junyang@pku.edu.cn)

<sup>2</sup> Previously at Dept. of the Geophysical Sciences, University of Chicago, Chicago, IL 60637, USA

<sup>3</sup> Laboratoire d'astrophysique de Bordeaux, Univ. Bordeaux, CNRS, B18N, allée Groffroy Saint-Hilaire, Pessac, F-33615, France

<sup>4</sup> Lab. for Atmospheric and Space Physics, University of Colorado in Boulder, CO 80303, USA

<sup>5</sup> Dept. of Atmospheric and Oceanic Sciences at McGill University, Montréal, QC, H3A 0G4, Canada

<sup>6</sup> Dept. of Earth, Atmospheric and Planetary Sciences, MIT, Cambridge, MA 02139, USA

<sup>7</sup> Lab. de Météorologie Dynamique, Institut Pierre Simon Laplace, CNRS, Paris, France

<sup>8</sup> Dept. of the Geophysical Sciences, University of Chicago, Chicago, IL 60637, USA

Received 2018 November 28; revised 2019 February 9; accepted 2019 February 21; published 2019 April 12

## Abstract

Robustly modeling the inner edge of the habitable zone is essential for determining the most promising potentially habitable exoplanets for atmospheric characterization. Global climate models (GCMs) have become the standard tool for calculating this boundary, but divergent results have emerged among the various GCMs. In this study, we perform an intercomparison of standard GCMs used in the field on a rapidly rotating planet receiving a G-star spectral energy distribution and on a tidally locked planet receiving an M-star spectral energy distribution. Experiments both with and without clouds are examined. We find relatively small difference (within 8 K) in global-mean surface temperature simulation among the models in the G-star case with clouds. In contrast, the global-mean surface temperature simulation in the M-star case is highly divergent (20–30 K). Moreover, even differences in the simulated surface temperature when clouds are turned off are significant. These differences are caused by differences in cloud simulation and/or radiative transfer, as well as complex interactions between atmospheric dynamics and these two processes. For example we find that an increase in atmospheric absorption of shortwave radiation can lead to higher relative humidity at high altitudes globally and, therefore, a significant decrease in planetary radiation emitted to space. This study emphasizes the importance of basing conclusions about planetary climate on simulations from a variety of GCMs and motivates the eventual comparison of GCM results with terrestrial exoplanet observations to improve their performance.

**Key words:** astrobiology – methods: numerical – planets and satellites: atmospheres – planets and satellites: general – radiative transfer

## 1. Introduction

The “habitable zone” is the circumstellar region where an Earthlike planet can support liquid water on its surface (Kasting et al. 1993, 2014; Kopparapu et al. 2013), which is essential for Earthlike life. The habitable zone concept has received increasing attention in recent years as the number of potentially habitable extrasolar planets has increased, and future NASA missions to characterize the atmospheres of potentially habitable extrasolar planets are being planned. This has led to the application of sophisticated three-dimensional (3D) global climate models (GCMs), which are capable of modeling atmospheric dynamics, clouds, and water vapor distributions, to the problem (e.g., Merlis & Schneider 2010; Edson et al. 2011; Pierrehumbert 2011; Leconte et al. 2013a, 2013b; Shields et al. 2013, 2014; Yang et al. 2013, 2014; Carone et al. 2014, 2015, 2016, 2017; Wang et al. 2014, 2016; Wolf & Toon 2014, 2015; Godolt et al. 2015; Way et al. 2015, 2017; Kopparapu et al. 2016, 2017; Popp et al. 2016; Turbet et al. 2016; Boutle et al. 2017; Haqq-Misra et al. 2017; Salameh et al. 2017; Wolf 2017; Wolf et al. 2017; Bin et al. 2018; Lewis et al. 2018; Turbet et al. 2018).

The inner edge of the habitable zone is marked by either a massive increase in surface temperature as a result of a fundamental limit on infrared emission to space by an Earthlike planet, the “runaway greenhouse,” or the loss of a planet’s

water through photodissociation and hydrodynamic escape due to high surface temperatures and a moist stratosphere, i.e. a “moist greenhouse” (Kasting 1988). Since modern Earth is relatively near the inner edge of the habitable zone (Kopparapu et al. 2013), aspects of these processes can be modeled using GCMs that were primarily designed to model the climate of modern and ancient Earth. In contrast, modeling the outer edge of the habitable zone requires accurate modeling of radiative transfer at high CO<sub>2</sub> concentrations, CO<sub>2</sub> clouds, and the dynamical effects of CO<sub>2</sub> condensation (Wordsworth et al. 2011; Wordsworth 2015; Turbet et al. 2016). As a result, more GCMs have been applied to the inner edge of the habitable zone, which has exposed the dramatic impact of differences in model formulations on its position.

GCMs generally disagree on the position of the inner edge of the habitable zone both for planets orbiting cool M stars and Sunlike G stars. For example, for a tidally locked planet orbiting an M star, Kopparapu et al. (2017) found that for a stellar temperature of 3400 K, updating the radiative scheme in the Community Atmosphere Model 4 (CAM4) GCM moved the inner edge of the habitable zone (runaway greenhouse) from 83% above modern Earth’s solar constant to 39% above it. Moreover, if we consider a planet with Earth’s rotation rate receiving the Sun’s spectral energy distribution, a runaway greenhouse occurs in the 3D Laboratoire de Météorologie Dynamique (LMD) Generic Model (LMDG) GCM when the

**Table 1**  
List of the GCMs in This Intercomparison

GCM	Resolution	Levels	Top Pressure	Dynamical Core
CAM3	$3.75^\circ \times 3.75^\circ$	26	3.0 hPa	Spectral
CAM4	$3.75^\circ \times 3.75^\circ$	26	3.0 hPa	Spectral
CAM4_Wolf	$4.0^\circ \times 5.0^\circ$	45	0.2 hPa	Spectral
AM2	$2.0^\circ \times 2.0^\circ$	32	2.2 hPa	Finite-volume
LMDG	$2.8^\circ \times 2.8^\circ$	30	1.0 hPa	Finite-difference

**Note.** The horizontal resolution is given as latitude by longitude. We also performed some CAM3 simulations with a  $2.8^\circ \times 2.8^\circ$  horizontal resolution, as well as CAM4 simulations with a  $1.9^\circ \times 1.9^\circ$  horizontal resolution and with a finite-volume dynamical core. Sensitivity tests using CAM3 with different model top pressures (0.9 and 0.1 hPa) showed that the model top pressure does not significantly influence the surface temperature.

solar constant is increased by 10% above modern Earth’s value (Leconte et al. 2013a), but has not occurred when it is increased by 15% in ECHAM6 (Popp et al. 2016) and by 21% in CAM4\_WOLF (Wolf & Toon 2015). These authors diagnosed differences in cloud simulation among their GCMs, but the lack of a uniform modeling framework made it impossible to firmly establish the cause of differences in cloud behavior, as well as whether variation in other processes might be important.

To clarify the situation, we organized a GCM intercomparison to investigate the causes of differences among GCMs that have been used to simulate the inner edge of the habitable zone in more detail. The participating GCMs are listed in Table 1. We started with a set of standardized 1D radiative calculations with assumed vertical profiles of temperature and water vapor and found that differences among the GCM radiative schemes in both the longwave and shortwave are mainly due to differences in water vapor absorption (Yang et al. 2016). LMDG had the strongest greenhouse (longwave) effect and CAM3 had the weakest, with a  $17 \text{ W m}^{-2}$  difference between them at a surface temperature of 320 K. In the shortwave, CAM4\_Wolf was the most absorptive<sup>9</sup> and CAM3 was the least, with a maximum top-of-atmosphere difference of  $\sim 10 \text{ W m}^{-2}$  for a G-star spectral energy distribution and  $\sim 20 \text{ W m}^{-2}$  for a M-star spectral energy distribution. The more sophisticated line-by-line radiative codes fell between these extremes in both the longwave and shortwave. When we combined both longwave and shortwave fluxes to estimate the effective stellar flux of the inner edge of the habitable zone, we found a variation of about 10% of modern Earth’s stellar flux among the GCMs due to differences in the treatment of water vapor radiative transfer alone.

The purpose of this paper is to extend the analysis of Yang et al. (2016) to the 3D effects of GCMs. We performed a set of standardized simulations for continent-free planets with (1) Earth’s rotation rate and the Sun’s spectral energy distribution and (2) a tidally locked orbital configuration and an idealized M-star spectral energy distribution (Section 2). We will investigate model variation in these simulations, as well as analyze additional simulations designed to identify differences between CAM3 (a cooler GCM), and LMDG (a warmer GCM) in more detail (Section 3). We conclude and discuss implications of this work in Section 4.

## 2. Methods

The GCMs studied in this intercomparison and their resolutions are displayed in Table 1. CAM3 is CAM version 3, developed at the National Center for Atmospheric Research (Collins 2002). CAM4 is CAM version 4 (Neale et al. 2010) and CAM4\_Wolf is CAM4 with a new radiative transfer module (<https://wiki.ucar.edu/display/etcam/Extraterrestrial+CAM>, see Wolf & Toon 2015). AM2 is a 3D GCM developed at the National Oceanic and Atmospheric Administration/Geophysical Fluid Dynamics Laboratory (GFDL 2004). LMDG is developed at LMD (Wordsworth et al. 2010a, 2010b, 2011; Forget et al. 2013).

We ran each GCM in a standard set of conditions. First, we ran them with a G-star spectral energy distribution, a 24 hr rotation period, 365 Earth days per year, and both with and without clouds. Second, we ran them with an M-star spectral energy distribution, tidally locked in a 1:1 synchronous rotation state, with a 60 day orbital and rotation period, and both with and without clouds. The G-star spectral energy distribution was the default distribution in the GCM for the Sun. The M-star spectral energy distribution was a blackbody Planck distribution corresponding to a temperature of 3400 K. AM2’s M star’s with-clouds experiment did not converge due to an unresolved problem, so it is not listed in the following figures or tables.

We used a stellar flux of  $1360 \text{ W m}^{-2}$ , zero obliquity, zero eccentricity, and Earth’s radius and gravity for all simulations. We ran the models in aqua-planet mode (with no continents) with a 50 m deep mixed layer ocean and no ocean heat transport. The atmosphere was 1 bar of  $\text{N}_2$  with 376 ppmv  $\text{CO}_2$  and a variable amount of  $\text{H}_2\text{O}$ . We set  $\text{CH}_4$ ,  $\text{N}_2\text{O}$ , CFCs,  $\text{O}_3$ ,  $\text{O}_2$ , and all aerosols to zero. We assumed no snow or sea ice, but allowed the sea surface temperature to drop below the freezing point. We set the surface albedo to 0.05 everywhere. We performed simulations both with clouds set to zero (more exactly, the radiative effects of clouds were turned off but cloud water and precipitation still formed) and with clouds calculated by the GCM cloud schemes. It should be noted here that because of the diversity of environments that have been modeled with LMDG, there are several possible cloud parameterizations available. Here, we use the cloud parameterization and parameters from Charnay et al. (2013), where the cloud particle size distributions for both liquid droplets and ice particles are fixed. Another important point is how the total cloud fraction of an atmospheric column—the one that will be used in the radiative transfer calculation—is computed from the cloud fractions at all of the modeled altitudes. In our baseline run (LMDG\_max), we assume that clouds have a maximal recovery probability, so that the total cloud fraction of the column is equal to the maximum cloud fraction at any altitude. We also present another set of simulations where we make the assumption that clouds at each level are uncorrelated, resulting in a random overlap (LMDG\_random). We also performed more detailed simulations using a CAM3 and LMDG run at a variety of stellar fluxes, and one example where we set water vapor to zero (a dry atmosphere) in both of these two models.

## 3. Results

### 3.1. G-star Planet GCM Comparison

Our first comparison involved planets in an orbital and rotational configuration similar to modern Earth’s, exposed to a G-star spectrum, with cloud radiative effects set to zero. As

<sup>9</sup> Wolf (2017) and Wolf et al. (2017) have corrected this bias by improving the wavelength resolution of the stellar spectrum and absorption coefficients.

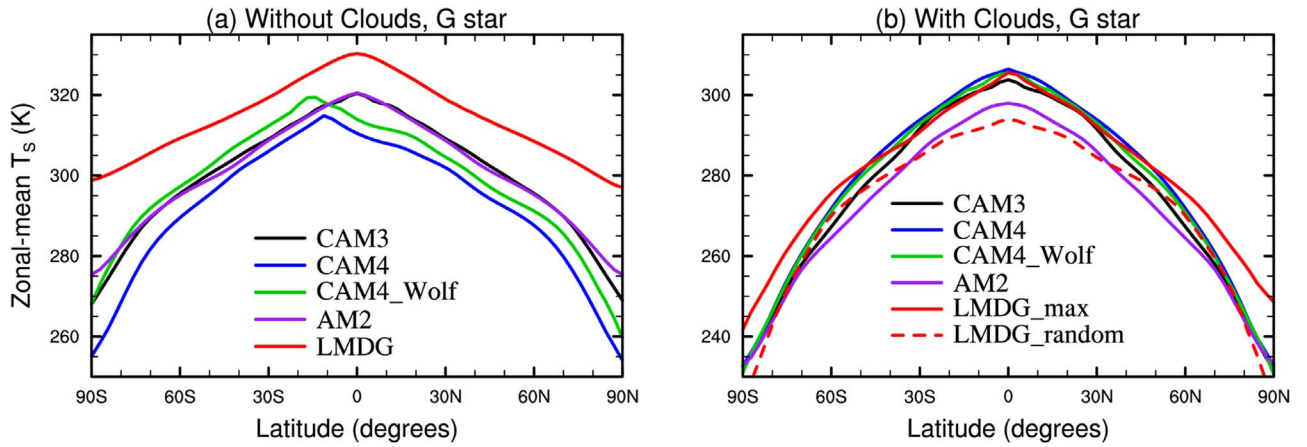


**Figure 1.** G-star surface temperature: zonal (east–west) mean surface temperature as a function of latitude for all GCMs both without clouds (a) and including clouds (b). The simulations assume a rapidly rotating aqua-planet with a G-star stellar spectrum and a stellar flux of  $1360 \text{ W m}^{-2}$ . LMDG\_max assumes a maximum overlap between different types of clouds at each altitude, while LMDG\_random employs a random overlap. Note the different y axis ranges between (a) and (b).

**Table 2**  
Global-mean Climatic Characteristics of the G-star Spectrum GCM Simulations

Simulations	GCMs	$T_s^a$ (K)	$\alpha_p^b$ [0–1]	SWCE <sup>c</sup> ( $\text{W m}^{-2}$ )	LWCE <sup>d</sup> ( $\text{W m}^{-2}$ )	NCE <sup>e</sup> ( $\text{W m}^{-2}$ )	Cld <sup>f</sup> (%)	WVP <sup>g</sup> ( $\text{kg m}^{-2}$ )	CWP <sup>h</sup> ( $\text{kg m}^{-2}$ )
No clouds	CAM3	307	0.10	...	...	...	...	100	...
	CAM4	301	0.10	...	...	...	...	62	...
	CAM4_Wolf	306	0.11	...	...	...	...	95	...
	AM2	307	0.10	...	...	...	...	99	...
	LMDG	319	0.11	...	...	...	...	178	...
With clouds	CAM4	290	0.32	–73	41	–32	70	34	0.20
	CAM3	287	0.33	–78	39	–39	77	25	0.18
	CAM4_Wolf	289	0.33	–74	34	–40	70	30	0.17
	AM2	282	0.35	–83	35	–48	86	15	0.08
	LMDG_max	290	0.30	–64	30	–34	43	24	0.15
	LMDG_random	282	0.39	–94	39	–55	86	12	0.13

**Notes.**

<sup>a</sup>  $T_s$ : global-mean surface temperature.

<sup>b</sup>  $\alpha_p$ : planetary albedo.

<sup>c</sup> SWCE: shortwave cloud radiative effect at the top of the model.

<sup>d</sup> LWCE: longwave cloud radiative effect at the top of the model.

<sup>e</sup> NCE: SWCE + LWCE.

<sup>f</sup> Cld: total cloud coverage.

<sup>g</sup> WVP: vertical-integrated water vapor content.

<sup>h</sup> CWP: vertical-integrated cloud water (liquid plus ice) content.

might be expected, differences in planetary albedo are small, within 0.01 (Table 2). This is consistent with the fact that the planetary albedos were fairly similar when the GCMs were run in 1D radiative-convective mode and forced with a G-star spectrum (see Figure 7 in Yang et al. 2016). Part of the explanation for this may also be that the surface albedo is very low (0.05) in our experiments, so that 95% of light hitting the surface is absorbed, and differences among the models in shortwave absorption by atmospheric water vapor can have less of an effect on the planetary albedo. Yang et al. (2016) have already pointed out significant differences in longwave radiative transfer that could result in different surface temperatures for a given shortwave heating, and this trend is confirmed here. Global-mean surface temperatures are within 1 K among CAM3, AM2, and CAM4\_Wolf, but are 6 K lower in CAM4 and  $\approx 12$  K higher in LMDG, which was the model

with the most pronounced greenhouse effect of water vapor (Figure 3(a) in Yang et al. 2016).

It should not be too surprising to find such significant differences in temperature simulation of the group without clouds, especially between LMDG and the other GCMs. Turning off clouds in our aqua-planet configuration with a surface albedo of 0.05 results in a bond albedo of  $\approx 0.10$ – $0.11$ , or equivalently a mean absorbed stellar flux of  $\approx 303$ – $306 \text{ W m}^{-2}$ . This is just at the limit where some 1D saturated radiative-convective models are in a runaway greenhouse, such as LMDG and CAM4\_Wolf, and others are not, such as CAM3 and CAM4 (see Figure 3(a) of Yang et al. 2016). Fortunately, atmospheric circulation-induced subsaturation in the subtropics makes all of the models in this experiment stable (Pierrehumbert 1995; Leconte et al. 2013b), but they are still functioning in a regime of high climate sensitivity due to the strong positive water vapor feedback. This



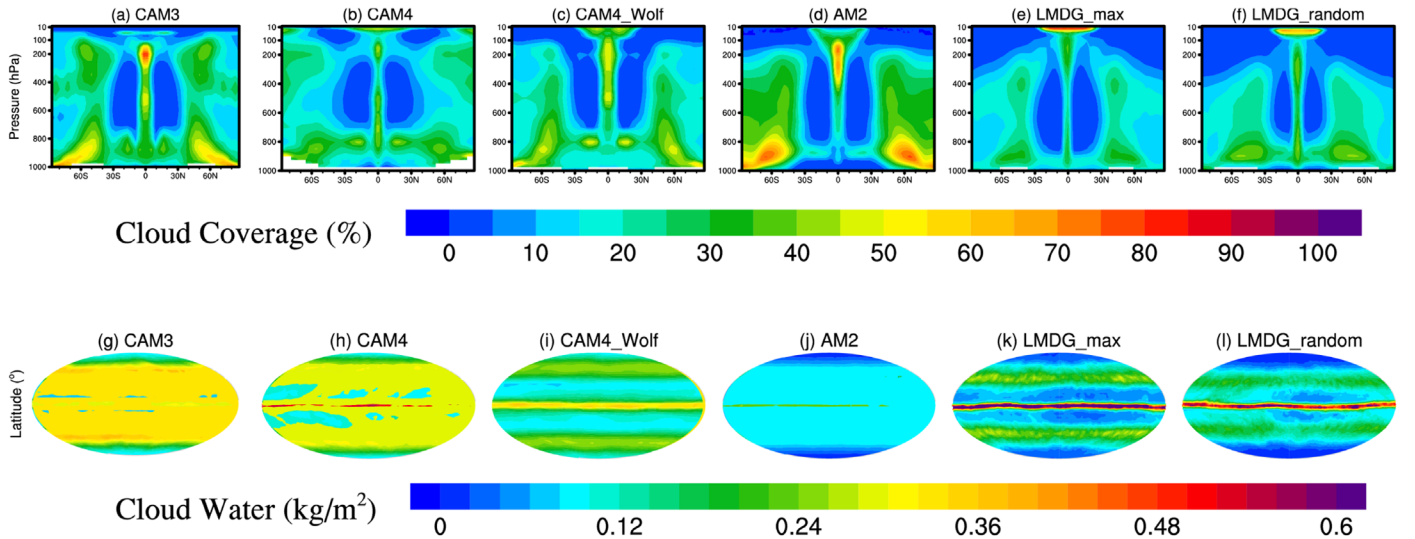


**Figure 2.** G-star clouds: top panels: contour plots of the zonal (east–west) mean cloud fraction as a function of latitude and pressure (vertical) and bottom panels: vertically integrated cloud water amount (including both liquid and ice phases) for all GCMs. The simulations assume a rapidly rotating aqua-planet with a G-star stellar spectrum and a stellar flux of  $1360 \text{ W m}^{-2}$ .

means that small variations in shortwave absorption can lead to large variations in surface temperature.

Interestingly, both CAM4 and CAM4\_Wolf exhibit spontaneous symmetry breaking in the cloud-free configuration, with a meridionally asymmetric climate resulting from symmetric boundary conditions (Figure 1(a)). Sensitivity tests using CAM4\_Wolf show that the hemisphere that contains the maximum in surface temperature depends on the initial conditions (figure not shown). The asymmetry results in a climate that is cooler than the other GCMs (Table 2), particularly in the case of CAM4, and foreshadows the important effects that differences in the simulation of atmospheric dynamics can produce in model climates in certain situations, which we will investigate further in Section 3.3.

Including clouds cools all models (Table 2 and Figure 1(b)), which is expected because clouds cool modern Earth. The global-mean net cloud radiative effect among the models varies greatly, from  $-32$  to  $-55 \text{ W m}^{-2}$ , mainly due to differences in the cloud fraction and cloud water amount parameterizations (Figure 2). The cloud radiative effect is more negative than its value on modern Earth ( $-20 \text{ W m}^{-2}$ ; Kiehl & Trenberth 1997), mainly because of the low surface albedo of a continent-free planet. Also, when clouds are included in the G-star spectrum calculations, meridional symmetry is restored to both CAM4 and CAM4\_Wolf (Figure 1(b)).

Interestingly, the global-mean surface temperature is more similar among the models when clouds are included than when they are not (Table 2). Part of the explanation for this may be that the models are cooler when clouds are included and, therefore, farther from the runaway greenhouse where the climate sensitivity is high. Additionally, all of the models have been tuned to reproduce the surface temperature of modern Earth, which is close to the regime simulated here. It may be that the cloud parameterizations are tuned to compensate for differences in clear-sky radiative transfer among the models.

It is important to note, however, that AM2 and LMDG\_random are both 5–8 K colder than the other models (Table 2). Given that AM2 produced very similar surface temperatures to CAM3 in the simulations without clouds, we can attribute the difference in simulations with clouds to differences in cloud

parameterization: the lower temperature is due to a stronger negative cloud radiative effect ( $-48 \text{ W m}^{-2}$ ), resulting in a higher planetary albedo. In fact, the cloud radiative effect at the top of the model is correlated with the surface temperature in all of the experiments, with a more negative cloud radiative effect associated with a lower global-mean surface temperature (Table 2). Similarly, the difference between LMDG\_max and LMDG\_random is entirely due to clouds and shows that in this configuration, switching from one extreme assumption on the cloud overlap to the other can have an 8 K effect on the global-mean surface temperature.

Spatial patterns of cloud fraction as well as cloud water amount are similar among the models, but the magnitudes have very large differences. All models show broadly similar patterns of cloud fractions, with pronounced intertropical convergence zones (ITCZs) and relatively low-level clouds at mid and high latitudes (Figures 2(a)–(f)). The cloud fraction is generally higher in AM2 than in the CAM models. This, in combination with potential microphysical differences (such as cloud particle size), is likely why AM2 produces a more negative cloud radiative effect and lower surface temperatures, although its cloud water amount is the lowest among the models (Figures 2(g)–(l)). CAM3 is slightly cloudier than CAM4 and CAM4\_Wolf, as was found by Wolf & Toon (2015), which likely causes its slightly lower global-mean surface temperature. The cloud fraction in LMDG\_max is less than that in LMDG\_random, while the cloud water amount is similar between the two versions of LMDG, so that clouds have a larger cooling effect in LMDG\_random:  $-55$  versus  $-34 \text{ W m}^{-2}$  (Table 2 and Figures 2(e)–(f) and (k)–(l)).

### 3.2. M-star Planet GCM Comparison

When we ran the GCMs in tidally locked configuration with an M-star spectrum, they produced larger differences than in the G-star case, even without clouds (Figure 3(a)). CAM3 produced the coolest climate, which is consistent with the fact that it has the weakest greenhouse effect in 1D radiative-transfer mode (Yang et al. 2016). CAM4\_Wolf is warmer than CAM3, CAM4, and AM2; a major cause of this is likely that

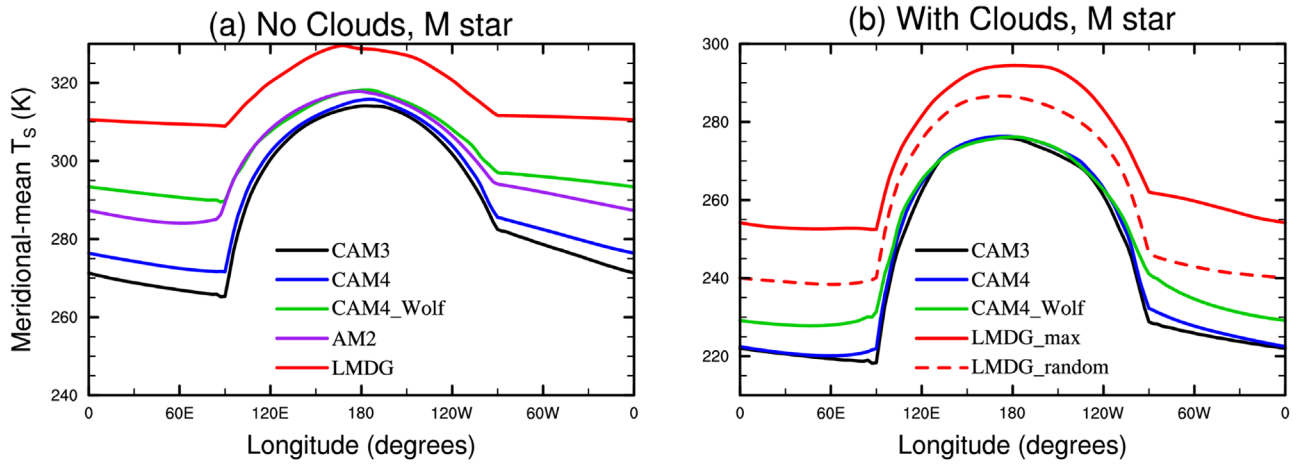


**Figure 3.** M-star surface temperature: meridional (north–south) mean surface temperature as a function of longitude for GCMs both without clouds ((a): CAM3, CAM4, CAM4\_Wolf, AM2, and LMDG) and including clouds ((b): CAM3, CAM4, CAM4\_Wolf, LMDG\_max, and LMDG\_random). The configuration assumes a tidally locked aqua-planet with an M-star stellar spectrum and a stellar flux of  $1360 \text{ W m}^{-2}$ . The substellar point is at  $180^\circ$  longitude. Note the different y axis ranges between (a) and (b).

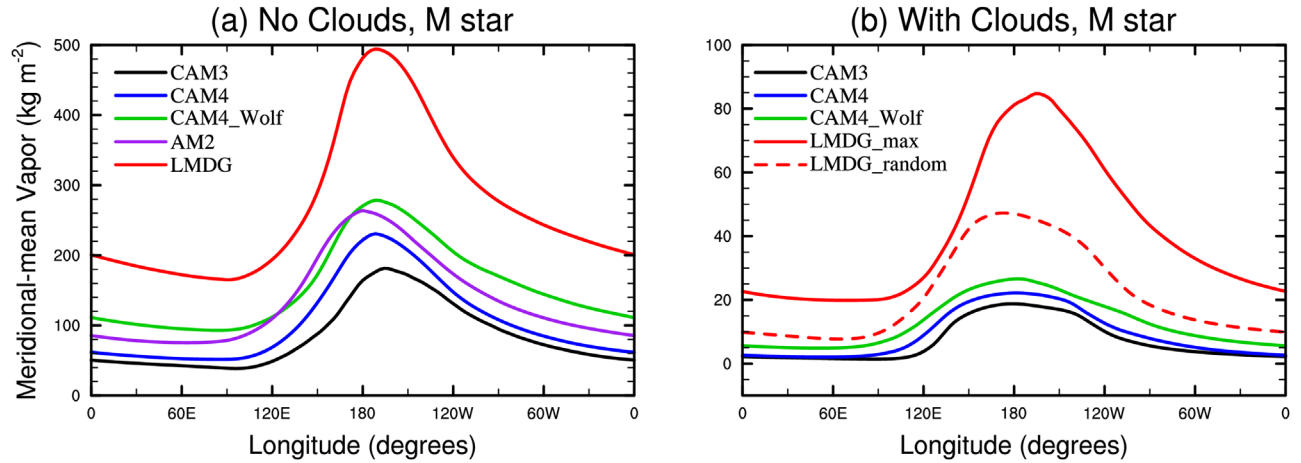


**Figure 4.** M-star water vapor content: meridional (north–south) mean vertically integrated water vapor content in the atmosphere as a function of longitude for GCMs both without clouds ((a): CAM3, CAM4, CAM4\_Wolf, AM2, and LMDG) and including clouds ((b): CAM3, CAM4, CAM4\_Wolf, LMDG\_max, and LMDG\_random). The configuration assumes a tidally locked aqua-planet with an M-star stellar spectrum and a stellar flux of  $1360 \text{ W m}^{-2}$ . Note the different y axis ranges between (a) and (b).

**Table 3**  
Global-mean Climatic Characteristics of the M-star Spectrum GCM Simulations

Simulations	GCMs	$T_s$ (K)	$\alpha_p$ [0-1]	SWCE ( $\text{W m}^{-2}$ )	LWCE ( $\text{W m}^{-2}$ )	NCE ( $\text{W m}^{-2}$ )	Cld (%)	WVP ( $\text{kg m}^{-2}$ )	CWP ( $\text{kg m}^{-2}$ )
No clouds	CAM3	288	0.04	...	...	...	...	84	...
	CAM4	291	0.04	...	...	...	...	106	...
	CAM4_Wolf	302	0.04	...	...	...	...	155	...
	AM2	299	0.04	...	...	...	...	136	...
	LMDG	316	0.04	...	...	...	...	268	...
With clouds	CAM3	246	0.46	-138	17	-121	97	7	0.15
	CAM4	247	0.46	-140	21	-119	98	9	0.17
	CAM4_Wolf	252	0.44	-131	19	-112	98	13	0.19
	LMDG_max	272	0.30	-82	20	-62	34	41	0.15
	LMDG_random	262	0.38	-108	22	-86	81	22	0.11

**Note.** For the notes of different variables, please see Table 2. An insolation of  $1360 \text{ W m}^{-2}$  is close to the runaway greenhouse of LMDG when cloud radiative effects are turned off, explaining the high temperature of the model. The with-clouds case of AM2 met one unresolved problem, so the experiment is not listed in the table.

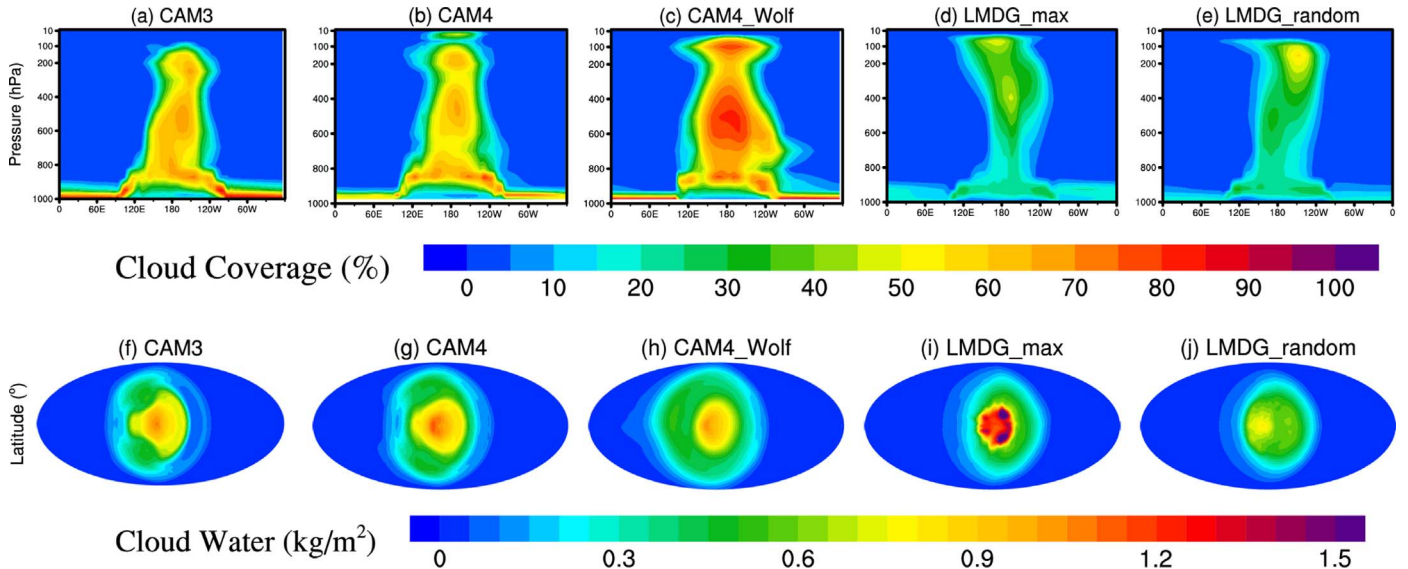


**Figure 5.** M-star clouds: top panels: contour plots of meridional (north–south) mean cloud fraction as a function of longitude and pressure (vertical), and bottom panels: vertically integrated cloud water amount (including both liquid and ice phases), for GCMs CAM3, CAM4, CAM4\_Wolf, LMDG\_max, and LMDG\_random. The configuration assumes a tidally locked aqua-planet with an M-star stellar spectrum and a stellar flux of  $1360 \text{ W m}^{-2}$ .

the greenhouse effect of water vapor in CAM4\_Wolf is the strongest among the four models (Yang et al. 2016). The CAM models and AM2 show a range of behavior, with differences in surface temperature among models particularly pronounced on the night side. This is likely due to the large changes in surface temperature that are possible if the strength of the night-side temperature inversion changes. This effect is leveraged by increases in the radiative timescale and atmospheric heat transport (Koll & Abbot 2016), due to larger water vapor concentration in warmer simulations. Parameterization of boundary layer turbulence could also influence the inversion strength and the night-side surface temperature. Moreover, the water vapor feedback acts to amplify the differences among models (Figure 4(a)). LMDG obtains the highest global-mean surface temperature in the no-cloud experiment, which is 14–28 K larger than other models (Table 3). As in the G-star, no-cloud experiment, although LMDG does not enter the runaway greenhouse at this insolation ( $1360 \text{ W m}^{-2}$ ), it is very close to the runaway greenhouse. The absorbed stellar energy of the system in this experiment is  $326 \text{ W m}^{-2}$  in global mean (the planetary albedo is 0.04).<sup>10</sup> Near or in the runaway greenhouse state, outgoing longwave radiation at the top of the atmosphere is insensitive to surface temperature and therefore a large increase in the surface temperature is required to balance even a very small increase in stellar radiation absorption (Pierrehumbert 2010).

A robust feature of these simulations is that, despite the lower albedo, all models are cooler in the tidally locked setup than in the rapidly rotating setup. This is mainly due to the radiator fin effect of the permanent night side of a tidally locked

orbit, which is relatively drier and can, therefore, emit longwave radiation to space more easily (Pierrehumbert 1995; Yang & Abbot 2014).

With clouds included, the various versions of CAM yield surprisingly similar surface temperatures (Figure 3(b)), especially given the variation in M-star spectral energy distribution stellar absorption in the 1D radiative-transfer mode (Yang et al. 2016), although CAM4\_Wolf does have a global-mean surface temperature about 5–6 K higher (Table 3). However, the global-mean surface temperature of LMDG is 10–26 K higher than those in CAM models. The remarkable divergence among models emphasizes the fact that we should not over-interpret the results of any single model when simulating exoplanet climates.

The most striking feature of the GCM cloud simulation in the M-star, tidally locked case (Figure 5) is that all models confirm previous work (Yang et al. 2013; Way et al. 2015; Kopparapu et al. 2016; Salameh et al. 2017) that predict deep convective clouds at the substellar point. We find that LMDG has relatively low cloud fractions that are somewhat weighted toward high-altitude, optically thin clouds (Figures 5(a)–(e)). This contributes significantly to the fact that LMDG produces much higher surface temperatures than the CAM models. The planetary albedos in LMDG\_max and LMDG\_random are 0.30 and 0.38, respectively, which are about 0.16 and 0.08 lower than those in CAM3 (Table 3). LMDG\_max has a much lower cloud fraction but a higher cloud water amount than LMDG\_random (Figures 5(d)–(e) and (i)–(j)), such that LMDG\_max has a weaker net cloud radiative effect,  $-62$  versus  $-86 \text{ W m}^{-2}$ , and a warmer surface, 272 versus 262 K in the global mean. Most models produce boundary layer clouds on the night side, but these have very little radiative effect. Again, the water vapor feedback is important for enhancing differences among models (Figure 4(b)).

### 3.3. Explaining Differences between CAM3 and LMDG

In order to investigate the mechanistic causes of differences among GCMs in more detail, we performed additional simulations and analyses of CAM3 (a relatively cool GCM), and LMDG (a relatively warm GCM). Figure 6 shows a

<sup>10</sup> Note that the runaway greenhouse limit depends on the orbital configuration of the planet. For example, in the lower-resolution LMG simulations described in Section 3.3, the absorbed stellar energy in the last converged solution is  $\approx 323 \text{ W m}^{-2}$  in the tidally locked, no-cloud configuration, but it is  $\approx 315 \text{ W m}^{-2}$  in the rapidly rotating, no-cloud configuration (Figure 6). The higher value in the tidally locked configuration is mainly due to the radiator fin effect of the permanent night side of a tidally locked orbit, which is relatively drier and can, therefore, emit longwave radiation to space more easily (Pierrehumbert 1995; Yang & Abbot 2014).



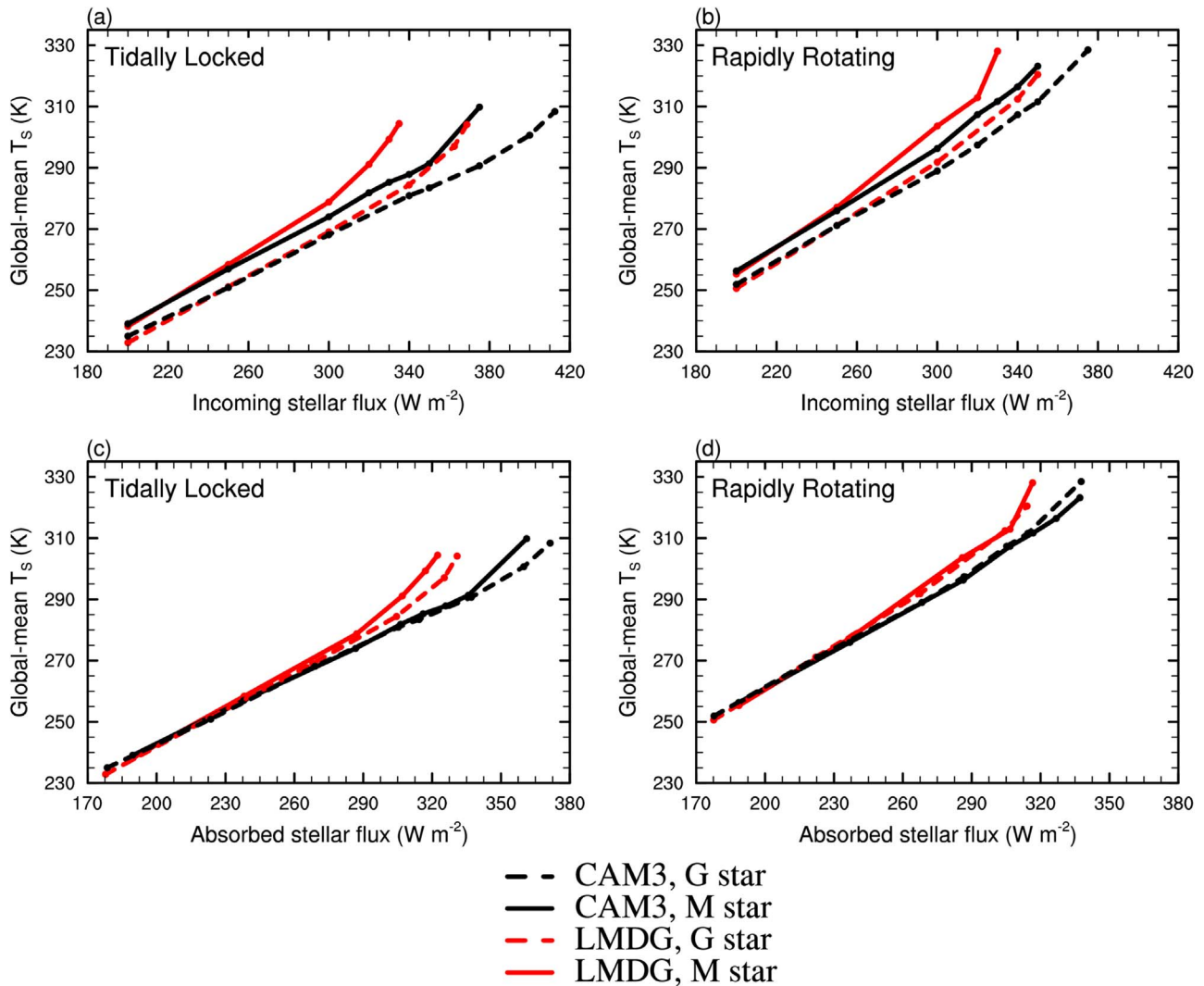


**Figure 6.** Global-mean surface temperature as a function of the global-mean incoming stellar flux ((a) and (b)) and absorbed stellar flux ((c) and (d)) for CAM3 (black lines) and LMDG (red lines) when the GCMs are run in a tidally locked aqua-planet configuration ((a) and (c)) and a rapidly rotating aqua-planet configuration ((b) and (d)) with a G-star stellar spectrum (dashed lines) and with an M-star stellar spectrum (solid lines). Clouds are turned off in all of these simulations, and the surface albedo is 0.05 everywhere. Note that the maximum stellar fluxes at the substellar point of the tidally locked experiments in (a) and (c) are  $1650 W m^{-2}$  (CAM3, G star),  $1500 W m^{-2}$  (CAM3, M star),  $1475 W m^{-2}$  (LMDG, G star), and  $1340 W m^{-2}$  (LMDG, M star), and of the rapidly rotating experiments in (b) and (d) are  $1500 W m^{-2}$  (CAM3, G star),  $1400 W m^{-2}$  (CAM3, M star),  $1400 W m^{-2}$  (LMDG, G star), and  $1320 W m^{-2}$  (LMDG, M star). A further increase of the stellar flux in LMDG will push LMDG into a runaway greenhouse state or cause CAM3 to blow up. Note: to speed up computations, we decreased the resolution of LMDG to  $11.25^\circ \times 5.625^\circ$  in the simulations for this figure. Although this will not affect the trends discussed here, it may affect the exact location of the runaway greenhouse limit of the model.

comparison of the global-mean surface temperature in CAM3 and LMDG as a function of both incoming stellar flux and absorbed stellar flux in both tidally locked and rapidly rotating aqua-planet configurations forced by both G-star and M-star spectral energy distributions. Clouds are set to zero in all of these simulations.

Both models are warmer for a given stellar flux when forced by an M-star spectral energy distribution because water vapor absorbs longer wavelengths of light better. Under the same incoming stellar flux, the global-mean surface temperature in the rapidly rotating case is higher than that in the tidally locked case. This is mainly due to the cooling effect of the radiator fin of the permanent night side on a tidally locked planet (Pierrehumbert 1995; Yang & Abbot 2014). When we plot as a function of absorbed stellar flux, the difference between G-star and M-star surface temperatures within a model is greatly reduced. By

plotting in this way though, a cold offset of CAM3 relative to LMDG appears, and the offset becomes larger with an increasing stellar flux. There are several processes that may cause the differences between CAM3 and LMDG, including radiative transfer, atmospheric dynamics, and differences in the water vapor distribution due to differences in convection parameterizations and dynamical processes. We will investigate these below, focusing our attention on the tidally locked case around an M star, where differences between the two models are largest.

### 3.3.1. Clear-sky Radiative Transfer

When forced by the same 1D temperature and water vapor profiles, CAM3 absorbs less radiation in both infrared and visible wavelengths than LMDG, i.e., CAM3 has a weaker greenhouse effect and smaller shortwave energy absorption (Yang et al. 2016). These differences result from LMDG using an updated

## LMDG vs CAM3 in Radiative Transfer (No Clouds, M star)

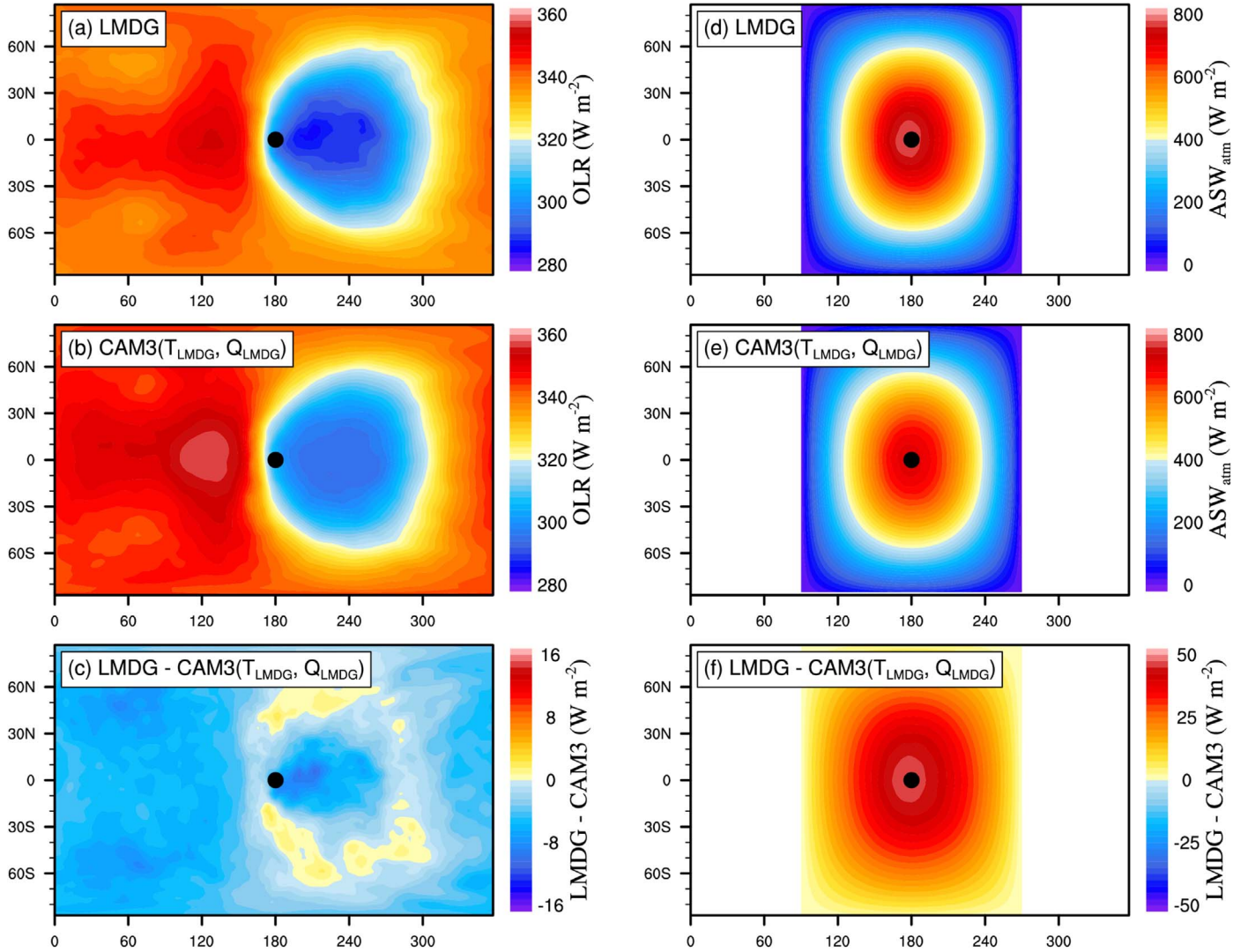


**Figure 7.** Cloud-free radiative transfer in LMDG and CAM3: outgoing longwave radiation (OLR) at the top of the model (left column) and absorbed shortwave flux by the atmosphere ( $ASW_{atm}$ ) for LMDG and for CAM3 forced by the same temperature and water vapor profiles from LMDG. (a) OLR in LMDG, (b) OLR in CAM3, and (c) the difference:  $LMDG - CAM3$ . (d)  $ASW_{atm}$  in LMDG, (e)  $ASW_{atm}$  in CAM3, and (f) the difference:  $LMDG - CAM3$ . The black dot is the substellar point. The global-mean value is  $-3.8 \text{ W m}^{-2}$  in (c) and  $11.7 \text{ W m}^{-2}$  in (f).

HITRAN database, HITRAN2008 versus HITRAN2000 in CAM3 (Yang et al. 2016). HITRAN2008 has many more absorption lines and stronger absorption cross sections in many wavelengths than HITRAN2000 (Supplementary Figure 3 in Goldblatt et al. 2013). Moreover, there are 36 stellar spectrum intervals in LMDG and only 7 in CAM3 (Yang et al. 2016). The higher spectral resolution in LMDG allows it to accurately resolve the individual absorption and window wavelengths separately. We confirm these differences here by inputting the simulated 3D temperature and water vapor profiles from LMDG into CAM3’s radiative transfer module (Figure 7). We find that the outgoing longwave radiation using CAM3’s radiation is higher than LMDG’s by  $3.8 \text{ W m}^{-2}$  in the global mean, and the absorbed shortwave radiation by the atmosphere using CAM3’s radiation is lower than LMDG’s by  $11.7 \text{ W m}^{-2}$  in the global mean. Both of these effects lead to a cooler climate in CAM3. Consistent with this finding, Kopparapu et al. (2017) showed that accounting for

these updated line lists and continuum absorption coefficients reduces the stellar flux limit for the runaway greenhouse.

### 3.3.2. Dry Dynamical Core

To test for dynamical differences between the two models, we performed tidally locked simulations with an M-star spectral energy distribution, no clouds, and with the atmospheric water vapor mixing ratio set to  $10^{-6}$  everywhere, which is the minimum vapor concentration covered by the radiative transfer correlated- $K$  tables in LMDG. The surface temperature simulation was nearly identical between the two models in this case (Figure 8); in fact, LMDG was actually slightly cooler than CAM3. This is in striking contrast to the same simulation performed with water vapor and clouds, where LMDG produced a climate much warmer than CAM3 (Table 3). This test shows that dry dynamics alone do not contribute



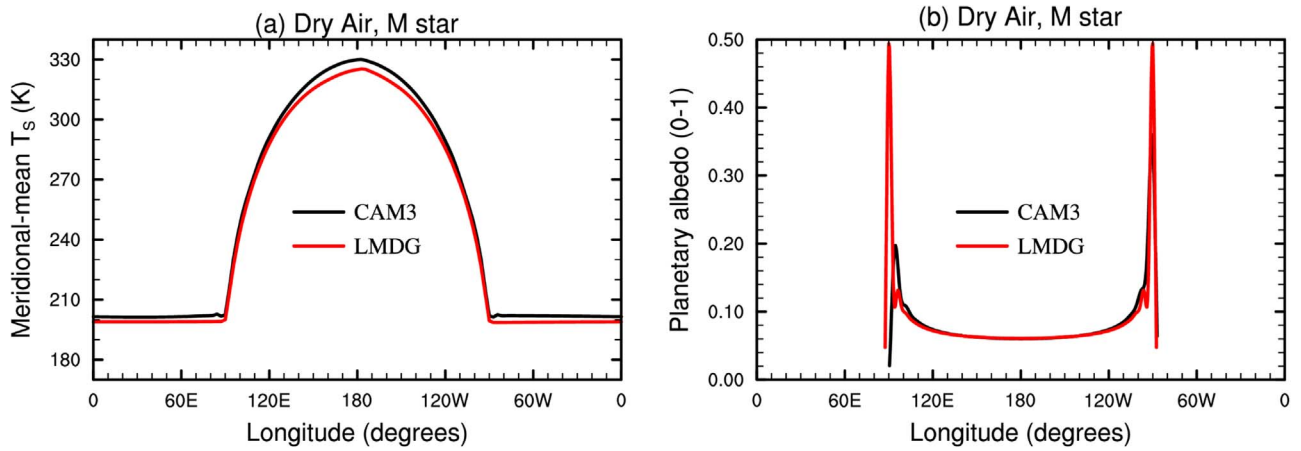


**Figure 8.** Dry atmosphere simulations: meridional (north–south) mean surface temperature (a) and planetary albedo (b) as a function of longitude for both CAM3 and LMDG, assuming a nearly dry atmosphere on a tidally locked planet with a stellar flux of  $1360 \text{ W m}^{-2}$ . The water vapor mixing ratio is set to  $10^{-6}$  everywhere, which is the minimum vapor concentration allowed in the radiative transfer correlated- $K$  tables of LMDG.

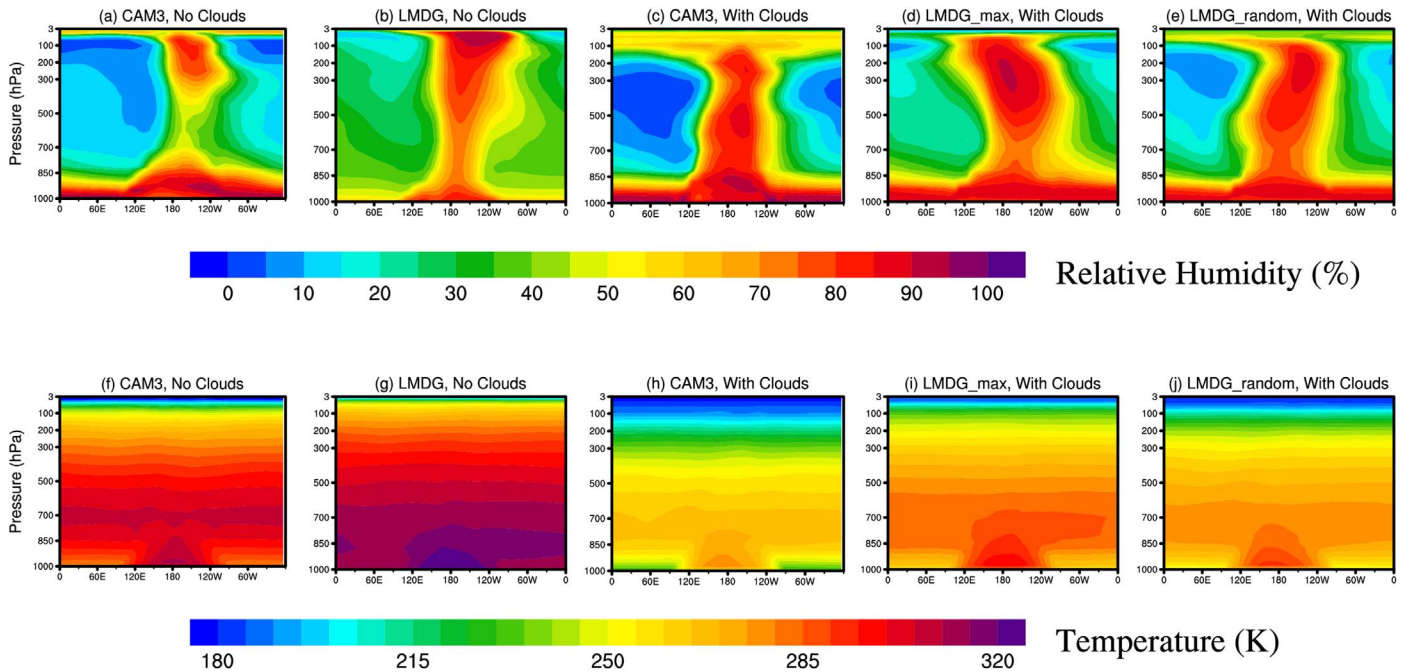


**Figure 9.** M-star relative humidity and air temperature: contour plots of meridional (north–south) mean relative humidity (top panels) and air temperature (bottom panels) as a function of longitude and pressure (vertical) for CAM3 and LMDG. The simulations are for a tidally locked aqua-planet with an M-star stellar spectrum and a stellar flux of  $1360 \text{ W m}^{-2}$ . Simulations both without clouds (a), (b), (f), and (g), and with clouds (c)–(e) and (h)–(j) are plotted.

significantly to differences in the simulation of climate in LMDG and CAM3.

### 3.3.3. Relative Humidity

We next turn our attention to the simulation of relative humidity (RH), which is defined as the percentage of water vapor mixing ratio<sup>11</sup> relative to the saturation water vapor mixing ratio (Wallace & Hobbs 2016; Abbot 2018) and is a critical term for inferring habitability (Pierrehumbert 1995;

<sup>11</sup> An alternative definition is the ratio of the vapor pressure to the saturation vapor pressure (such as Wallace & Hobbs 2016). The American Meteorological Society (AMS) uses the vapor pressure to define RH, while the World Meteorological Organization (WMO) used the mixing ratio to define RH ([http://glossary.ametsoc.org/wiki/Main\\_Page](http://glossary.ametsoc.org/wiki/Main_Page)). The differences between these two definitions are very small when the water vapor is diluted.

Leconte et al. 2013b; Pierrehumbert & Ding 2016) that can be affected by both radiative transfer and atmospheric dynamics. RH is higher in LMDG than in CAM3 at high altitudes around the planet, both with and without clouds (Figure 9). High-altitude water vapor is particularly important because it increases the optical thickness in a cold region of the atmosphere, causing strong greenhouse warming. The fact that the high-altitude RH is much higher in LMDG than in CAM3 is likely one of the causes of the much higher surface temperature in LMDG.

Atmospheric RH is determined by many processes, including large-scale atmospheric circulation, eddies, and small-scale processes, such as convection, entrainment, detrainment, re-evaporation of rain droplets, and diffusion (Pierrehumbert et al. 2007; Sherwood et al. 2010; Wright et al. 2010). Here, we can

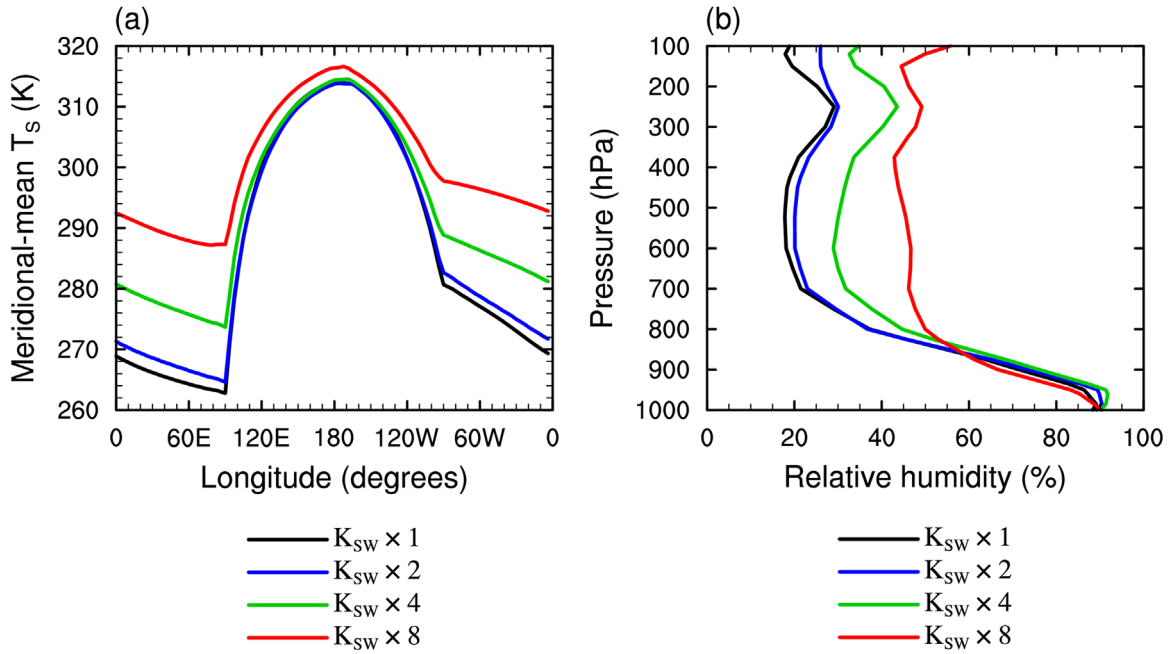


**Figure 10.** Varying the shortwave absorption coefficient of water vapor ( $K_{\text{H}_2\text{O}}$ ) in CAM3: meridional (north–south) mean surface temperature as a function of longitude (left) and global-mean vertical profiles of relative humidity (right) for the simulations with  $K_{\text{H}_2\text{O}}$  increased by a multiple of 1, 2, 4, or 8. The simulations are for a tidally locked aqua-planet with an M-star stellar spectrum, a stellar flux of  $1292 \text{ W m}^{-2}$ , and without clouds. The surface albedo is set to zero everywhere, so that the planetary albedo is close to zero in all of these cases (not shown). Note that the four and eight times absorption coefficients are unrealistic. Increasing the absorption coefficients by about twice in CAM3 can approximately match the shortwave heating rates in LMDG (see Figure 11 below).

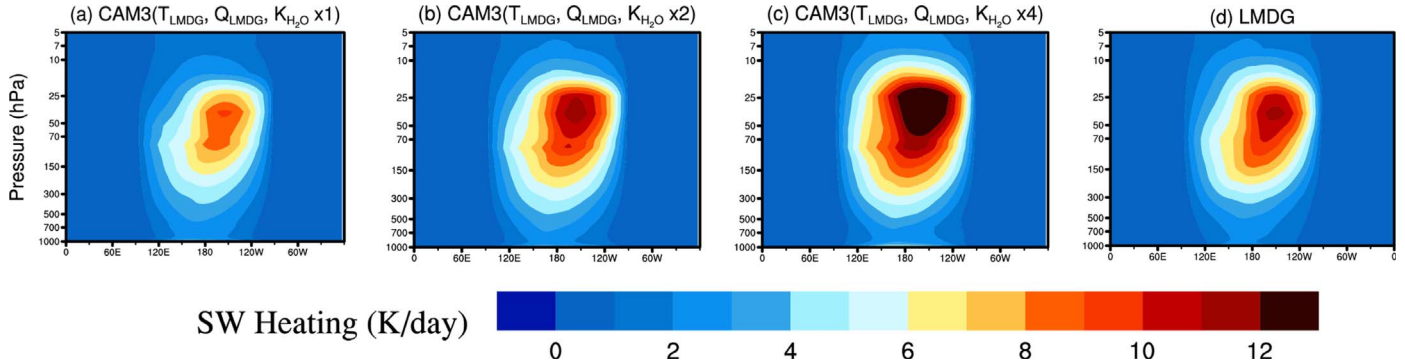


**Figure 11.** Meridional (north–south) mean shortwave heating rate: CAM3 vs. LMDG. (a) Using CAM3’s default shortwave absorption coefficient of water vapor ( $K_{\text{H}_2\text{O}}$ ), (b) doubling the values of  $K_{\text{H}_2\text{O}}$ , (c) quadrupling the values of  $K_{\text{H}_2\text{O}}$ , and (d) LMDG. In the calculations, CAM3’s radiative transfer module is forced by temperature and water vapor profiles from LMDG. The calculations are for a tidally locked aqua-planet with an M-star stellar spectrum, a stellar flux of  $1360 \text{ W m}^{-2}$ , and without cloud radiative effects.

identify two factors that likely make LMDG moister. The first is that LMDG uses a forced convective adjustment (Manabe & Wetherald 1967) to calculate the atmospheric lapse rate, whereas CAM3 determines the atmospheric lapse rate prognostically based on complex moist processes (Wolf & Toon 2015). This difference can have a big impact on moisture distributions, as Wolf & Toon (2015) found when they compared LMDG and CAM4\_Wolf, which determines the lapse rate in a similar way to CAM3. Specifically, they showed that in hot climates, even under the same global-mean surface temperature, LMDG’s upper atmosphere is always much moister than CAM4\_Wolf’s. Next, we suggest a second reason LMDG may be moister: differences in shortwave absorption.

A major difference between CAM3 and LMDG is that absorption of stellar radiation by water vapor is significantly higher in LMDG than in CAM3 (Section 3.3.1). When we artificially increased the shortwave water vapor absorption

coefficient in CAM3, we found that this significantly increased the high-altitude RH and surface temperature (Figure 10). When we doubled the absorption coefficient by water vapor, the shortwave heating rate of the atmosphere in CAM3 is close to that in LMDG (Figure 11), the global-mean surface temperature increases by 0.9 K, and the night-side surface temperature increases by 2.5 K.<sup>12</sup> In CAM4\_Wolf, we find the same phenomenon: when the shortwave water vapor absorption coefficient is decreased, the high-altitude RH decreases, and the surface cools (Figure 12). To understand this, we built a last saturation model for water vapor (Pierrehumbert et al. 2007) in which we trace air parcels and approximate their specific humidity as its value the last time the parcel was saturated (see the Appendix). Model resolution and

<sup>12</sup> Although seemingly small, this effect would be further amplified by the strong positive water vapor radiative feedback if another source of heating—an increase in longwave absorption, for example—were to be added.

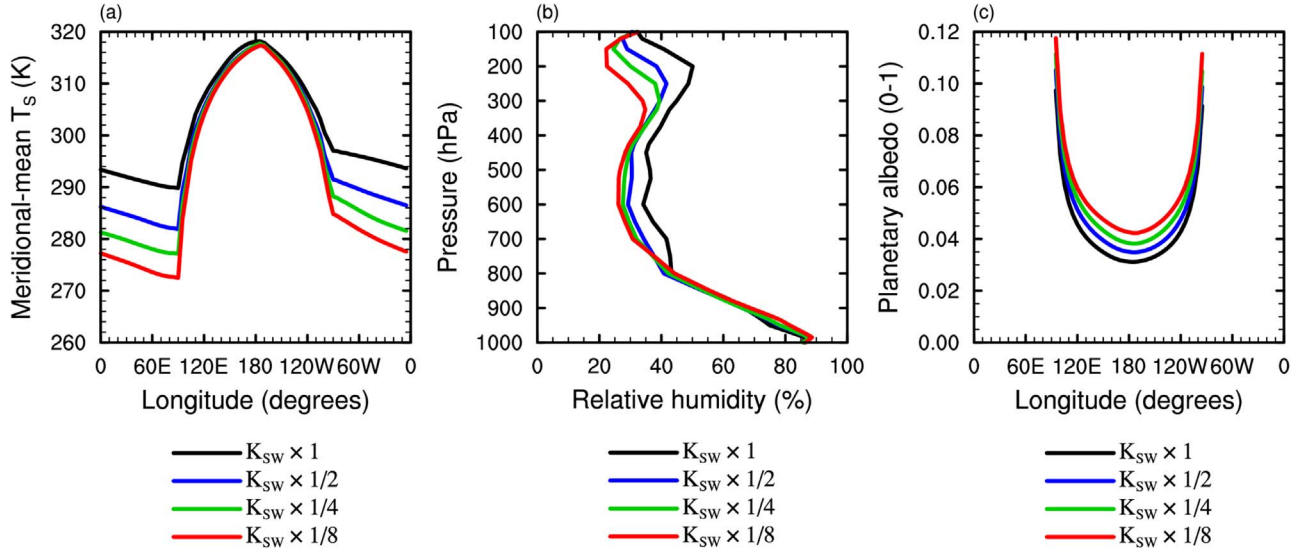


**Figure 12.** Varying the shortwave absorption coefficient of water vapor ( $K_{\text{H}_2\text{O}}$ ) in CAM4. Wolf: meridional (north–south) mean surface temperature (a) and planetary albedo (c) as a function of longitude, and global-mean vertical profiles of relative humidity (b) for the simulations with  $K_{\text{H}_2\text{O}}$  decreased by a multiple of 1, 1/2, 1/4, or 1/8. The simulations are for a tidally locked aqua-planet with an M-star stellar spectrum, a stellar flux of  $1360 \text{ W m}^{-2}$ , and without clouds. The global-mean surface temperatures are 302, 297, 295, and 292 K, and the planetary albedos are 0.044, 0.049, 0.053, and 0.057, respectively. The surface albedo is 0.05 everywhere. The tiny changes in planetary albedo are not enough to explain the changes in surface temperature.

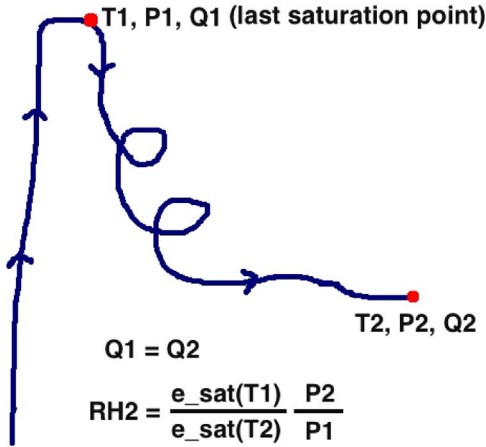


**Figure 13.** Schematic illustration of the last saturation model for an air parcel. Specific humidity is conserved after the time of last saturation.  $T$  represents the air parcel’s temperature,  $P$  its pressure, and  $Q$  its specific humidity.

numerical diffusion limit the accuracy of this method, but we are able to broadly reproduce the high-altitude RH.

As air parcels rise in convection in the substellar region, they tend to experience detrainment and convective outflow at some pressure associated with an anvil cloud. This will mark the point of last saturation, as the air is subsequently advected away from the substellar point and descends to higher pressures as it cools radiatively and heats adiabatically. As shown in Figure 13, for a given pressure in the descending region ( $P_2$ ), the relative humidity ( $RH_2$ ) is determined by the temperature, and the air pressure at the last saturation point ( $T_1$  and  $P_1$ ), and can be approximately written as,

$$\begin{aligned}
 RH_2 &= 100 \frac{e(T_2)}{e_{\text{sat}}(T_2)} \frac{P_2 - e_{\text{sat}}(T_2)}{P_2 - e(T_2)} \approx 100 \frac{e(T_2)}{e_{\text{sat}}(T_2)} \\
 &\approx 100 \left( \frac{e_{\text{sat}}(T_1)}{e_{\text{sat}}(T_2)} \right) \times \left( \frac{P_2}{P_1} \right), \quad (1)
 \end{aligned}$$

where  $e_{\text{sat}}$  is the saturation vapor pressure,  $e$  is the vapor pressure, and we assumed the vapor pressure is much less than the air pressure at and after the last saturation. It has previously been shown that the Fixed Anvil Temperature (FAT) hypothesis (Hartmann & Larson 2002; Kuang & Hartmann 2007; Thompson et al. 2016) holds fairly well for convection near the substellar point of tidally locked simulations in CAM3 (Yang & Abbot 2014). This implies that the temperature of the point of last saturation ( $T_1$ ) and the corresponding saturation vapor pressure ( $e_{\text{sat}}(T_1)$ ) should stay roughly constant<sup>13</sup> as we increase the shortwave water vapor absorption coefficient, but the pressure ( $P_1$ ) should decrease due to surface warming and an increase in the altitude of the anvil cloud. This is exactly what we see in CAM3 (Figure 14). Since the temperature at last saturation ( $T_1$ ) does not change much as the shortwave water vapor absorption coefficient is increased, the saturation vapor pressure ( $e_{\text{sat}}(T_1)$ ) does not change much. But the air pressure ( $P_1$ ) decreases, so the specific humidity at last saturation must increase. Another way to explain this is that there is the same amount of water vapor (same temperature), but much less dry air (lower pressure), so the water vapor specific humidity increases. This means the RH will be higher all along the air

<sup>13</sup> The FAT hypothesis denotes that the temperature at the detrainment level of tropical convective anvil clouds is nearly constant during climate change. The underlying mechanism is that energy balance in the tropical troposphere is primarily between convective heating by latent heat release in regions of deep convection and radiative cooling by longwave emission to space in clear-sky regions with large-scale subsidence. Because of this, the detrainment level of anvil clouds should be located at the altitude where the clear-sky radiative cooling diminishes rapidly. The clear-sky radiative cooling rate in the upper troposphere is primarily determined by water vapor emission. The temperature at which the saturation water vapor pressure becomes small enough that water vapor emission is ineffective is constrained by local air temperature because of the Clausius–Clapeyron relationship. Therefore, the temperature at the top of anvil clouds should be nearly independent of surface temperature. For the simulations without clouds in our study, we turn off the cloud radiative effects but cloud formation, latent heat release, precipitation, and clear-sky radiative transfer still exist, so that the FAT hypothesis works in our simulations.



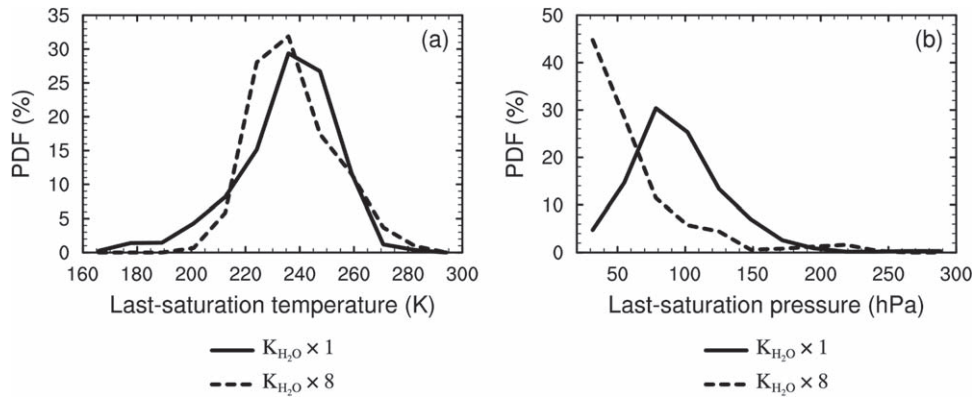


**Figure 14.** Probability distribution functions (PDFs) of the last saturation temperature ((a),  $T_1$  in Figure 13) and pressure ((b),  $P_1$  in Figure 13) for CAM3 run with the normal shortwave water vapor absorption coefficient  $K_{\text{H}_2\text{O}}$  (solid) and with eight times  $K_{\text{H}_2\text{O}}$  (dashed).

parcel’s subsequent trajectory, and it explains why increasing the shortwave water vapor absorption coefficient increases the high-altitude RH throughout the planet.

In addition to the shortwave water vapor absorption coefficient, we have tested the sensitivity of CAM3 to a number of other parameters. These include: numerical momentum diffusion near the top of the model (0.1 or 100 times of the default value), surface momentum transfer coefficient (0.1 or 10 times of the default value), sensible and latent heat exchange coefficients (0.5 or 2 times of the default value), deep and shallow convection relaxation timescales (from 0.1 to 16 hr), deep and shallow convection precipitation efficiencies (0.1 or 10 times of the default value), deep convection downdraft mass flux factor (from 0 to 0.7), the RH limit for large-scale condensation (from 50% to 99.9%), convective and large-scale precipitation evaporation efficiencies (0.1 or 10 times of the default value), and the critical Richardson number for planetary boundary mixing (from 0.1 to 1). In all of these tests, the global-mean surface temperature in the cloud-free, M-star, tidally locked configuration is within the range of 286–294 K, indicating that varying one single parameter can induce a global-mean surface temperature difference within 8 K. More work would be required to test the effect of varying two or more parameters simultaneously.

### 3.3.4. Summary

To summarize, there are a number of differences between LMDG and CAM3 that lead to CAM3 simulating a much colder climate for tidally locked, M-star planets. Differences in the models’ radiative schemes lead to LMDG absorbing more stellar radiation and emitting less planetary radiation to space. The interplay between atmospheric dynamics and cloud parameterization leads to a higher cloud fraction and cloud optical thickness at the substellar point in CAM3, causing significant cooling. Finally, moist processes and the interplay between the absorption of stellar radiation and atmospheric dynamics leads to higher RH at high altitudes in LMDG, and, therefore, lower planetary thermal radiation to space, causing significant warming of LMDG.

## 4. Conclusion and Discussion

In this paper, we performed an intercomparison of the 3D global climate models CAM3, CAM4, CAM4\_Wolf, AM2, and LMDG both with and without clouds. Our conclusions are as follows:

1. When running with clouds for rapidly rotating planets receiving a G-star spectral energy distribution and a stellar flux of  $1360 \text{ W m}^{-2}$ , the models produce global-mean surface temperatures within 8 K. Small differences in cloud parameterization assumptions can lead to this level of variation, as shown by the LMD\_max and LMD\_random simulations.
2. When running with clouds for tidally locked planets receiving an M-star spectral energy distribution and a stellar flux of  $1360 \text{ W m}^{-2}$ , the GCM’s behavior is much more divergent (up to 26 K in global-mean surface temperature). LMDG\_max is much warmer than the other models. Clouds are an important part of the reason for this behavior, but large differences among the models with clouds set to zero demonstrate that model divergence is also due to clear-sky radiative effects of water vapor, as well as the interaction of radiation with atmospheric dynamics.
3. We implemented a last saturation model for RH and used it to show that a larger shortwave water vapor absorption in GCM leads not only to direct warming by decreasing the planetary albedo, but also to indirect warming by increasing the high-altitude RH around the planet and, therefore, decreasing planetary radiation emitted to space (increasing the greenhouse effect).

Besides of the differences in surface temperature, air temperature, and RH between the models, there are also significant differences in stratospheric water vapor concentration (Figure 15), which influences the onset of the moist greenhouse state and the location of the inner edge of the habitable zone. From this figure, one could find that the stratospheric water vapor concentration is not directly connected to surface temperature, but that it is more directly determined by air temperatures at high altitudes. The surface temperature difference among the models in the M-star, tidally locked experiments is larger than in the G-star, rapidly rotating experiments, but the stratospheric water vapor difference above 30 hPa is smaller in the former group of experiments. The strength of stratospheric circulation, such as the Brewer-Dobson circulation on Earth, can also influence the stratospheric water vapor (Holton et al. 1995; Danielsen 1993; Fueglistaler & Haynes 2005; Romps & Kuang 2009). Future work is required to analyze the differences in stratospheric circulation and troposphere–stratosphere water vapor exchange between the models.

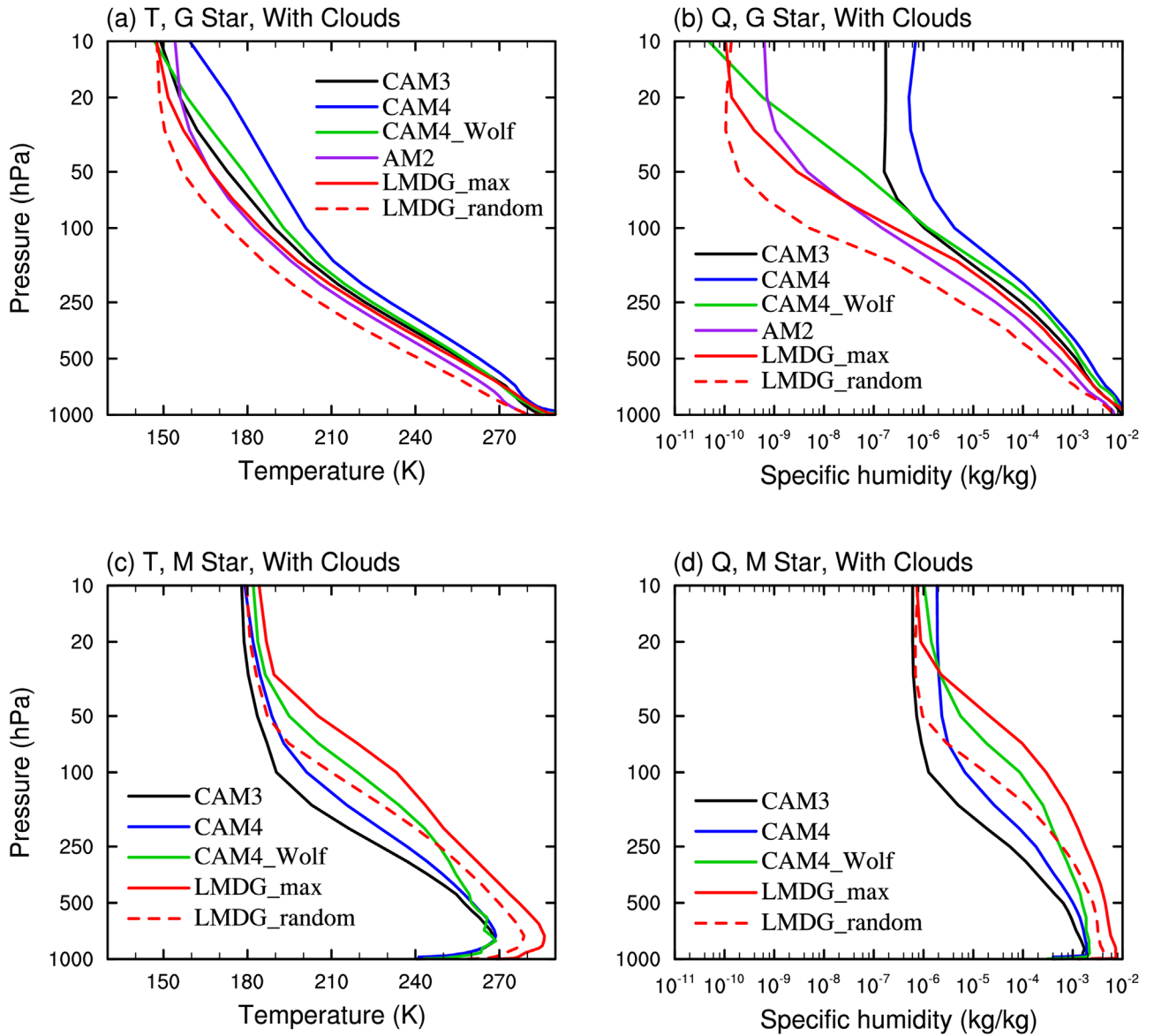


**Figure 15.** Global-mean temperature profiles (a) and (c) and specific humidity profiles (b) and (d). (a) and (b): simulations assume a rapidly rotating aqua-planet with a G-star stellar spectrum, a stellar flux of  $1360 \text{ W m}^{-2}$ , and clouds. (c) and (d): simulations assume a tidally locked aqua-planet with an M-star stellar spectrum, a stellar flux of  $1360 \text{ W m}^{-2}$ , and clouds. No ozone is included in all of the simulations.

Our results are useful for explaining the differences between models that have been employed to examine the location of the inner edge of the habitable zone, such as why LMDG enters a runaway greenhouse state in a lower stellar radiation than that in the CAM models (Leconte et al. 2013a; Yang et al. 2013; Wolf & Toon 2015). Moreover, our results suggest that future work in developing exoplanet climate models should focus on improving the radiative transfer of water vapor in both the longwave and shortwave and updating the cloud parameterization. In the present GCMs, the accuracy in shortwave radiative transfer is lower than that in longwave radiative transfer. Before direct atmospheric observations of exoplanets, laboratory cloud experiments and high-resolution cloud resolving models could be employed to investigate the clouds under different planetary parameters, and the results could be used to improve the cloud parameterization in GCMs. When interpreting the differences and similarities among the models considered here, it is important to emphasize that agreement

among some or most of the GCMs does not imply that the climates they simulate are correct. This is particularly true for the CAM models, which share a similar heritage, and, therefore, share many similar or identical subroutines. Determining which GCMs are the most accurate requires detailed comparison with observations from Earth, other solar system planets, and eventually observations of exoplanets. We should also remember that a GCM might perform better in one context and worse in another.

Since we performed the simulations for this intercomparison, three new planetary GCMs have been developed: Resolving Orbital and Climate Keys of Earth and Extraterrestrial Environments with Dynamics (ROCKE-3D; Way et al. 2017), the Met Office Unified Model (UM; Boutle et al. 2017), and Isca (Vallis et al. 2018), as well as others. Readers should be aware of these models and future intercomparison efforts should include them.

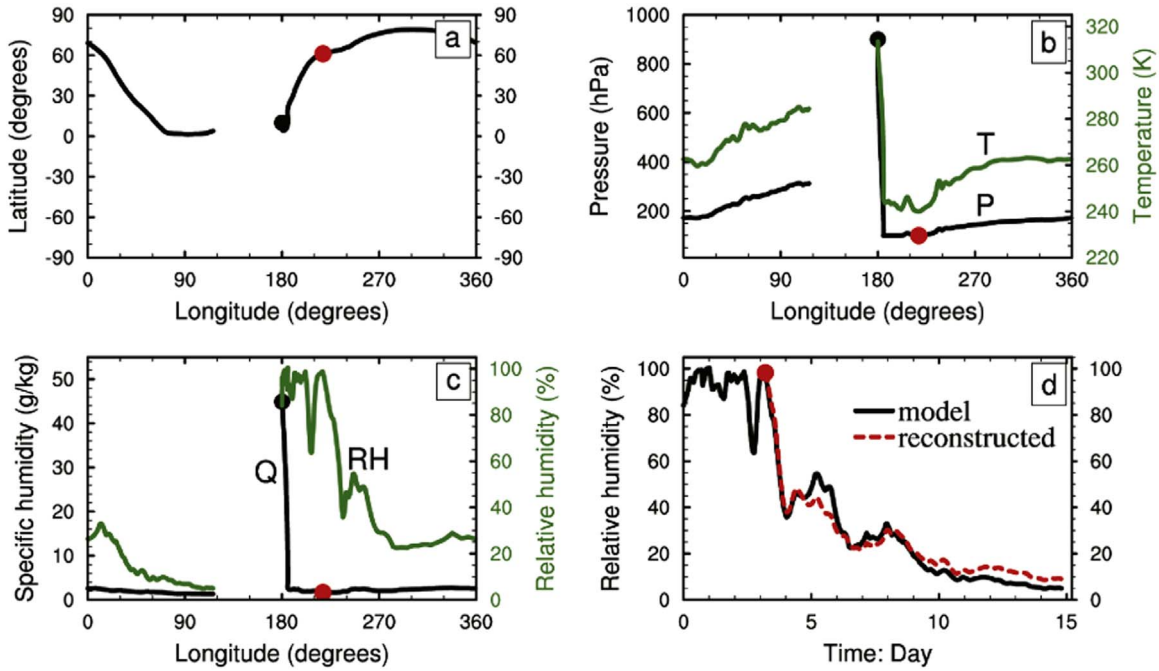


**Figure 16.** This is an example of the trajectory of an air parcel that we trace using the last saturation model. The black dot in all panels shows where we begin to trace the parcel, and the red dot shows where it last reaches saturation. Panel (a) shows the latitude and longitude of the parcel as it rises near the substellar point and is advected away from the substellar point at altitude. Panel (b) shows the air pressure and temperature of the parcel as a function of longitude as it makes its voyage. Last saturation is achieved at the coldest air temperature reached. Panel (c) shows the specific and relative humidities of the parcel as a function of longitude. Panel (d) shows the GCM relative humidity (black line) and the relative humidity reconstructed from the last saturation model (red line) as a function of time. The red dot has a relative humidity of 90% rather than 100% (same as Wright et al. 2010); this is because of the large grid size of the GCM (about 300 km), which means much of the air would saturate when the grid-mean relative humidity is 90%. The substellar point is at  $0^\circ$  latitude and  $180^\circ$  longitude.

We acknowledge support from NASA grant number NNX16AR85G, which is part of the “Habitable Worlds” program and from the NASA Astrobiology Institutes Virtual Planetary Laboratory, which is supported by NASA under cooperative agreement NNX15ZDA001C. J.Y. acknowledges support from the National Science Foundation of China (NSFC) grants 41861124002, 41675071, 41606060, and 41761144072. J.L. acknowledges that this project has received funding from the European Research Council (ERC) under the European Unions Horizon 2020 research and innovation program (grant agreement No. 679030/WHIPLASH). We are grateful to Junyan Xiong for his help in drawing Figures 13 and 16. This work was completed in part with resources provided by the University of Chicago Research Computing Center.

### Appendix Last Saturation Model

This appendix briefly describes the last saturation model we built for RH in the GCM CAM3 based on the method of

Pierrehumbert et al. (2007). The model works by tracking an air parcel as it moves around the planet and assuming that its specific humidity is conserved after it reaches saturation for the last time (Figure 13). This model does not include processes such as numerical diffusion that can occur in the GCM. In a tidally locked planet, last saturation generally occurs when convective ascent at the substellar point ceases. The air parcel then flows away from the substellar point and descends as it cools radiatively and heats adiabatically. We can see these processes occurring in Figure 16, which shows the trajectory of an example parcel and the RH, and we can infer for it using the last saturation method. The last saturation model is able to reproduce the broad pattern of high-altitude RH as simulated by CAM3 (Figure 17). In particular, the model reproduces the low RH on the night side, with approximately the correct magnitude. As would be expected for a model without numerical diffusion, the RH field from the last saturation model is somewhat more noisy than that from CAM3.



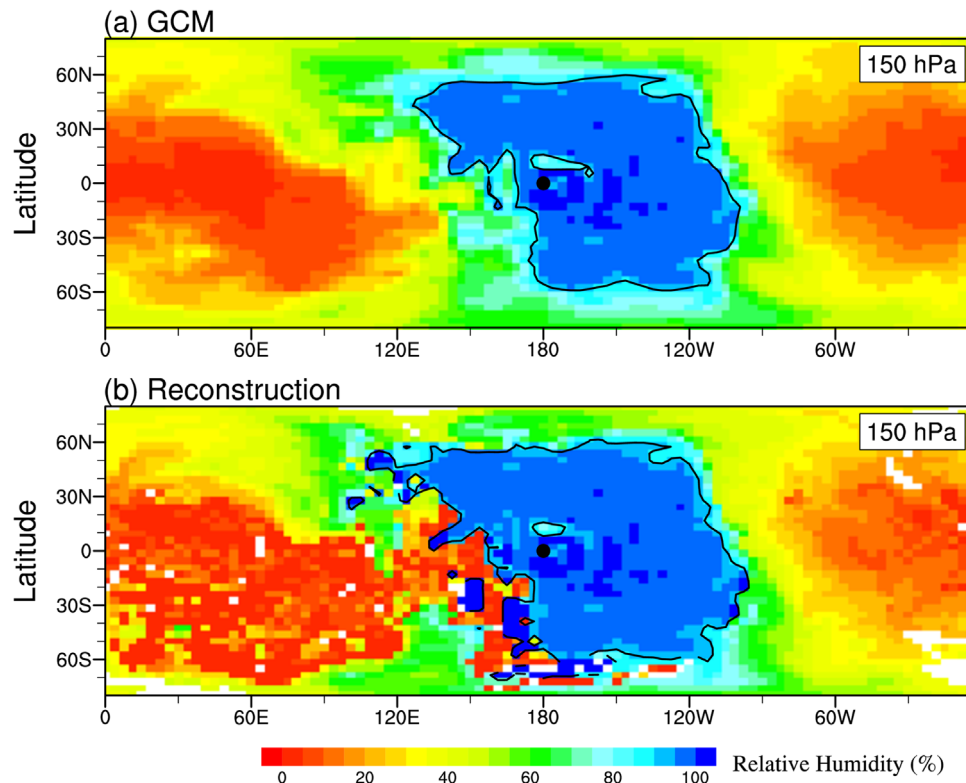


**Figure 17.** High-altitude (150 hPa) relative humidity from GCM (a) is compared to the reconstructed relative humidity using the last saturation model (b) in a model snapshot. The white spots in the last saturation model represent areas that no air parcel we traced ended up at this particular time snapshot. The model is run in tidally locked aqua-planet configuration and forced with an M-star spectral energy distribution. The black dot is the substellar point, and the black line is the contour of a relative humidity of 90%.

### ORCID iDs

Jun Yang <https://orcid.org/0000-0001-6031-2485>

Jérémy Leconte <https://orcid.org/0000-0002-3555-480X>

Eric T. Wolf <https://orcid.org/0000-0002-7188-1648>

Timothy Merlis <https://orcid.org/0000-0002-5593-8210>

Daniel D. B. Koll <https://orcid.org/0000-0002-9076-6901>

Dorian S. Abbot <https://orcid.org/0000-0001-8335-6560>

### References

- Abbot, D. S. 2018, 182, arXiv:1806.04481
- Bin, J., Tian, F., & Liu, L. 2018, *PSPS*, **492**, 121
- Boutle, I. A., Mayne, N. J., Drummond, B., et al. 2017, *A&A*, **601**, A120
- Carone, L., Keppens, R., & Decin, L. 2014, *MNRAS*, **445**, 930
- Carone, L., Keppens, R., & Decin, L. 2015, *MNRAS*, **453**, 2412
- Carone, L., Keppens, R., & Decin, L. 2016, *MNRAS*, **461**, 1981
- Carone, L., Keppens, R., Decin, L., & Henning, T. 2017, *MNRAS*, **473**, 4672
- Charnay, B., Forget, F., Wordsworth, R., et al. 2013, *JGRD*, **118**, 10414
- Collins, W. D. 2002, Description of the NCAR Community Atmosphere Model (CAM3), 189, <http://www.cesm.ucar.edu/models/atm-cam/#documentation>
- Danielsen, E. F. 1993, *JGR*, **98**, 8665
- Edson, A., Lee, S., Bannon, P., Kasting, J. F., & Pollard, D. 2011, *Icar*, **212**, 1
- Forget, F., Wordsworth, R. D., Millour, E., Madeleine, J.-B., & Charnay, B. 2013, *Icar*, **222**, 81
- Fueglistaler, S., & Haynes, P. H. 2005, *JGRD*, **110**, D24108
- GFDL 2004, *JCLI*, **17**, 4641
- Godolt, M., Grenfell, J. L., Hamann-Reinus, A., et al. 2015, *P&SS*, **111**, 62
- Goldblatt, C., Robinson, T. D., Zahnle, K. J., & Crisp, D. 2013, *NatGeo*, **6**, 661
- Haqq-Misra, J., Wolf, E., Joshi, M., et al. 2017, *ApJ*, **852**, 1
- Hartmann, D. L., & Larson, K. 2002, *GeoRL*, **29**, 1951
- Holton, J. R., Haynes, P. H., McIntyre, M. E., et al. 1995, *RvGeo*, **33**, 403
- Kasting, J. F. 1988, *Icar*, **74**, 472
- Kasting, J. F., Kopparapu, R. K., Ramirez, R. M., & Harman, C. E. 2014, *PNAS*, **111**, 12641
- Kasting, J. F., Whitmire, D. P., & Reynolds, R. T. 1993, *Icar*, **101**, 108
- Kiehl, J. T., & Trenberth, K. E. 1997, *BAMS*, **78**, 197
- Koll, D. D. B., & Abbot, D. S. 2016, *ApJ*, **825**, 99
- Kopparapu, R. K., Ramirez, R., Kasting, J. F., et al. 2013, *ApJ*, **765**, 131
- Kopparapu, R. K., Wolf, E. T., Arney, G., et al. 2017, *ApJ*, **845**, 5
- Kopparapu, R. K., Wolf, E. T., Haqq-Misra, J., et al. 2016, *ApJ*, **819**, 84
- Kuang, Z., & Hartmann, D. L. 2007, *JCh*, **20**, 2051
- Leconte, J., Forget, F., Charnay, B., et al. 2013a, *A&A*, **554**, A69
- Leconte, J., Forget, F., Charnay, B., Wordsworth, R., & Pottier, A. 2013b, *Natur*, **504**, 268
- Lewis, N. T., Lambert, F. H., Boutle, I. A., et al. 2018, *ApJ*, **854**, 1
- Manabe, S., & Wetherald, R. 1967, *JATs*, **24**, 241
- Merlis, T. M., & Schneider, T. 2010, *JAMES*, **2**, 13
- Neale, R. B., Richter, J. H., Conley, A. J., et al. 2010, Description of the NCAR Community Atmosphere Model (CAM 4.0), [http://www.cesm.ucar.edu/models/ccsm4.0/cam/docs/description/cam4\\_desc.pdf](http://www.cesm.ucar.edu/models/ccsm4.0/cam/docs/description/cam4_desc.pdf)
- Pierrehumbert, R. T. 1995, *JATs*, **52**, 1784
- Pierrehumbert, R. T. 2010, Principles of Planetary Climate (Cambridge: Cambridge Univ. Press)
- Pierrehumbert, R. T. 2011, *ApJL*, **726**, L8
- Pierrehumbert, R. T., Brogniez, H., & Roca, R. 2007, in The Global Circulation of the Atmosphere, ed. T. Schneider & A. H. Sobel (Princeton, NJ: Princeton Univ. Press), 143
- Pierrehumbert, R. T., & Ding, F. 2016, *RSPSA*, **2190**, 1
- Popp, M., Schmidt, H., & Marotzke, J. 2016, *NatCo*, **7**, 10627
- Romps, D., & Kuang, Z. 2009, *GeoRL*, **36**, L09804
- Salameh, J., Popp, M., & Marotzke, J. 2017, *CIDy*, **50**, 2395
- Sherwood, S. C., Roca, R., Weckwerth, T. M., & Andronova, N. G. 2010, *RvGeo*, **48**, 1
- Shields, A. L., Bitz, C. M., Meadows, V. S., Joshi, M. M., & Robinson, T. D. 2014, *ApJL*, **785**, L9
- Shields, A. L., Meadows, V. S., Bitz, C. M., et al. 2013, *AsBio*, **13**, 715
- Thompson, D. W. J., Bony, S., & Li, Y. 2016, *PNAS*, **114**, 8181
- Turbet, M., Bolmont, E., Leconte, J., et al. 2018, *A&A*, **612**, 22
- Turbet, M., Leconte, J., Selsis, F., et al. 2016, *A&A*, **596**, A112

- Vallis, G. K., Colyer, G., Geen, R., et al. 2018, [GMD](#), **11**, 843
- Wallace, J. M., & Hobbs, P. V. 2016, *Atmospheric Science: An Introductory Survey* (London: Academic), 504
- Wang, Y., Feng, T., & Hu, Y. 2014, [ApJL](#), **791**, L12
- Wang, Y., Liu, Y., Feng, T., et al. 2016, [ApJL](#), **823**, L20
- Way, M., Del Genio, A., Kelley, M., Aleinov, I., & Clune, T. 2015, arXiv:1511.07283
- Way, M. J., Aleinov, I., Amundsen, D. S., et al. 2017, [ApJS](#), **231**, 12
- Wolf, E., & Toon, O. 2014, [GeoRL](#), **41**, 167
- Wolf, E., & Toon, O. 2015, *JGR*, **120**, 5775
- Wolf, E. T. 2017, [ApJL](#), **839**, L1
- Wolf, E. T., Shields, A. L., Kopparapu, R. K., Haqq-Misra, J., & Toon, O. B. 2017, [ApJ](#), **837**, 107
- Wordsworth, R., Forget, F., & Eymet, V. 2010a, [Icar](#), **210**, 992
- Wordsworth, R., Forget, F., Selsis, F., et al. 2010b, [A&A](#), **522**, A22
- Wordsworth, R. D., Forget, F., Selsis, F., et al. 2011, [ApJL](#), **733**, L48
- Wordworth, R. 2015, [ApJ](#), **808**, 1
- Wright, J. S., Sobel, A., & Galewsky, J. 2010, [JCLI](#), **23**, 4556
- Yang, J., & Abbot, D. S. 2014, [ApJ](#), **784**, 155
- Yang, J., Boué, G., Fabrycky, D. C., & Abbot, D. S. 2014, [ApJL](#), **787**, L2
- Yang, J., Cowan, N. B., & Abbot, D. S. 2013, [ApJL](#), **771**, L45
- Yang, J., Leconte, J., Wolf, E. T., et al. 2016, [ApJ](#), **826**, 222